The Nature of the Stochastic Wind Forcing of ENSO

Antonietta Capotondi and Prashant D. Sardeshmukh

University of Colorado, Cooperative Institute for Research in Environmental Sciences, and NOAA/Earth System Research Laboratory, Physical Sciences Division, Boulder, Colorado

Lucrezia Ricciardulli

Remote Sensing Systems, Santa Rosa, California

(Manuscript received 9 December 2017, in final form 14 May 2018)

ABSTRACT

El Niño–Southern Oscillation (ENSO) is commonly viewed as a low-frequency tropical mode of coupled atmosphere–ocean variability energized by stochastic wind forcing. Despite many studies, however, the nature of this broadband stochastic forcing and the relative roles of its high- and low-frequency components in ENSO development remain unclear. In one view, the high-frequency forcing associated with the subseasonal Madden–Julian oscillation (MJO) and westerly wind events (WWEs) excites oceanic Kelvin waves leading to ENSO. An alternative view emphasizes the role of the low-frequency stochastic wind components in directly forcing the low-frequency ENSO modes. These apparently distinct roles of the wind forcing are clarified here using a recently released high-resolution wind dataset for 1990–2015. A spectral analysis shows that although the high-frequency winds do excite high-frequency Kelvin waves, they are much weaker than their interannual counterparts and are a minor contributor to ENSO development. The analysis also suggests that WWEs should be viewed more as short-correlation events with a flat spectrum at low frequencies that can efficiently excite ENSO modes than as strictly high-frequency events that would be highly inefficient in this regard. Interestingly, the low-frequency power of the rapid wind forcing is found to be higher during El Niño than La Niña events, suggesting a role also for state-dependent (i.e., multiplicative) noise forcing in ENSO dynamics.

1. Introduction

Tropical Pacific winds play a key role in the development and decay of ENSO events. In particular, El Niño initiation and growth rely on the Bjerknes feedback (Bjerknes 1969), whereby westerly wind anomalies develop over the central equatorial Pacific Ocean in response to warm eastern Pacific sea surface temperature (SST) anomalies and sustain and enhance the original SST perturbation.

In addition to the low-frequency wind variations associated with this low-frequency air–sea coupling, tropical winds also have stochastic components that are important in forcing ENSO events. Previous studies (e.g., Roulston and Neelin 2000; Zavala-Garay et al. 2008) have found that the stochastic wind forcing has a broadband spectrum ranging from subseasonal to interannual periods. However, it is still unclear which part of this spectrum is most influential in ENSO growth. Many studies (Zhang and Gottschalck 2002; Roundy and Kiladis 2006, among others) have stressed the importance of subseasonal frequency forcing in this regard, specifically through wind variations associated with the Madden–Julian oscillation (MJO) with periods between 30 and 90 days exciting oceanic Kelvin waves in the same frequency range and triggering ENSO. Several studies have also stressed the role of fast wind fluctuations known as westerly wind events (WWEs) in triggering El Niño conditions. Such events, with durations between a few days and a few weeks, can also excite downwelling oceanic equatorial Kelvin waves that deepen the thermocline in the eastern Pacific and create sufficiently large SST anomalies to initiate the Bjerknes feedback (McPhaden et al. 1988; McPhaden 1999). Pulses of easterly wind anomalies, known as easterly wind events (EWEs), have similarly been claimed to be important in the development of La Niña events (Chiodi and Harrison 2015).

Corresponding author: Dr. Antonietta Capotondi, antonietta.capotondi@noaa.gov

DOI: 10.1175/JCLI-D-17-0842.1

Of particular relevance to us here is that WWEs and EWEs are often perceived as high-frequency wind variations at the high-frequency tail of the subseasonal band (e.g., Lengaigne et al. 2004; Puy et al. 2016). However, the wind events are often defined as zonal wind anomalies from the annual cycle exceeding certain duration and amplitude thresholds [see Puy et al. (2016) for a list of definitions] and are not frequency band limited. This mismatch between definition and perception has added to the confusion regarding the role of such wind events in ENSO dynamics, as we argue in this paper.

As shown in section 4, the high-frequency wind variations are strongly modulated by the interannual signal, a significant fraction of which is associated with the deterministic wind response to large-scale SST anomalies. The commonly used definitions of WWEs and EWEs convolve such deterministic and stochastic components of the winds and create further confusion about the causes of individual ENSO events.

In contrast to studies that have emphasized the high-frequency wind variations as potentially important triggers of ENSO, other studies have stressed the role of the low-frequency (interannual) components of the stochastic wind fluctuations in forcing ENSO variability. Roulston and Neelin (2000) used an intermediate coupled model of the tropical Pacific to examine the relative roles of forcing in different frequency bands, and found that only the low-frequency component of the stochastic forcing could efficiently excite ENSO variability in their model. They attributed the origin of this low-frequency wind forcing (“climate noise” in their terminology) to oceanic memory outside the tropical Pacific, since it was computed as a residual after removing the wind component linearly related to the large-scale SST anomaly field within the tropics.

Other studies have associated the low-frequency component of the stochastic forcing with the rectification of subseasonal SST anomalies through nonlinear evaporative cooling and zonal advection (Kessler and Kleeman 2000), with the rectification of zonal wind stress due to its quadratic dependence on winds (Rong et al. 2011), and with the slow-amplitude modulation of the atmospheric noise forcing by the slowly evolving SST anomalies themselves (Eisenman et al. 2005; Gebbie et al. 2007; Levine and Jin 2017; Levine et al. 2017). Indeed, some modeling studies (Lengaigne et al. 2004) have shown that inserting a WWE into a coupled model simulation can trigger additional stronger WWEs that are displaced eastward, consistent with the observed evolution of the 1997/98 El Niño event (McPhaden 1999), thus effectively producing a low-frequency envelope of WWE activity.

The lack of clarity on the relative importance of the subseasonal versus interannual components of the wind forcing of ENSO, signifying apparently different roles for nonlinear versus linear processes in ENSO dynamics, is partly due to the confusion between strictly high-frequency forcing and forcing with a short correlation time scale. While the former has power only at subseasonal frequencies, the latter has power also at the interannual end of the spectrum, which is the only frequency range relevant for ENSO if the dynamics of ENSO are effectively linear and stochastically forced (Penland and Sardeshmukh 1995; Newman and Sardeshmukh 2017). We illustrate this basic but important point in section 2 using the simplest two-component linear model with slow and fast components.

Section 3 describes the observational datasets used in this study. In section 4 we present the spectral characteristics of the equatorial winds and examine their evolution in the subseasonal and interannual frequency bands as well as their relationship with SST and sea surface height (SSH) variations. We also provide evidence for the state dependency of the magnitude of the stochastic wind components. A summary and conclusions follow in section 5.

2. Stochastic versus high-frequency forcing

Consider the simplest dynamical framework of a slow variable (e.g., SST) driven by a fast variable (e.g., wind) in a linear model of the form:

$$dx_s/dt = -\lambda_s x_s + a x_f(t) \quad \text{and} \tag{1a}$$

$$dx_f/dt = -\lambda_f x_f + b w(t), \tag{1b}$$

where x_s and x_f are slow and fast variables defined by their correlation time scales $\tau_s = \lambda_s^{-1}$ and $\tau_f = \lambda_f^{-1}$, respectively, with $\tau_s \gg \tau_f$. The fast variable x_f forces the slow variable x_s and is itself forced by the white noise forcing $w(t)$. Specifying $\tau_s = 8$ months and $\tau_f = 6.3$ days yields the power spectra of x_s and x_f in Figs. 1a and 1b. The spectra in variance preserving form (Fig. 1b) show that the largest power of x_s is at periods around $2\pi\tau_s$ ($\sim$4 years) and of x_f is at periods around $2\pi\tau_f$ ($\sim$40 days), representative of ENSO and MJO periods, respectively. As Fig. 1a shows, the fast variable x_f has appreciable power even at low frequencies, and an approximately flat white spectrum at periods longer than $\sim 2\pi\tau_f$. Sample time series of x_f (Fig. 1e) and x_s (Fig. 1d) from a time integration of the model show the appreciable amplitudes of both. However, if x_s is forced instead with a strictly high-pass filtered version of this sample time series of x_f (turquoise line in Fig. 1e) with periods shorter than 100 days (shaded areas in Figs. 1a and 1b),

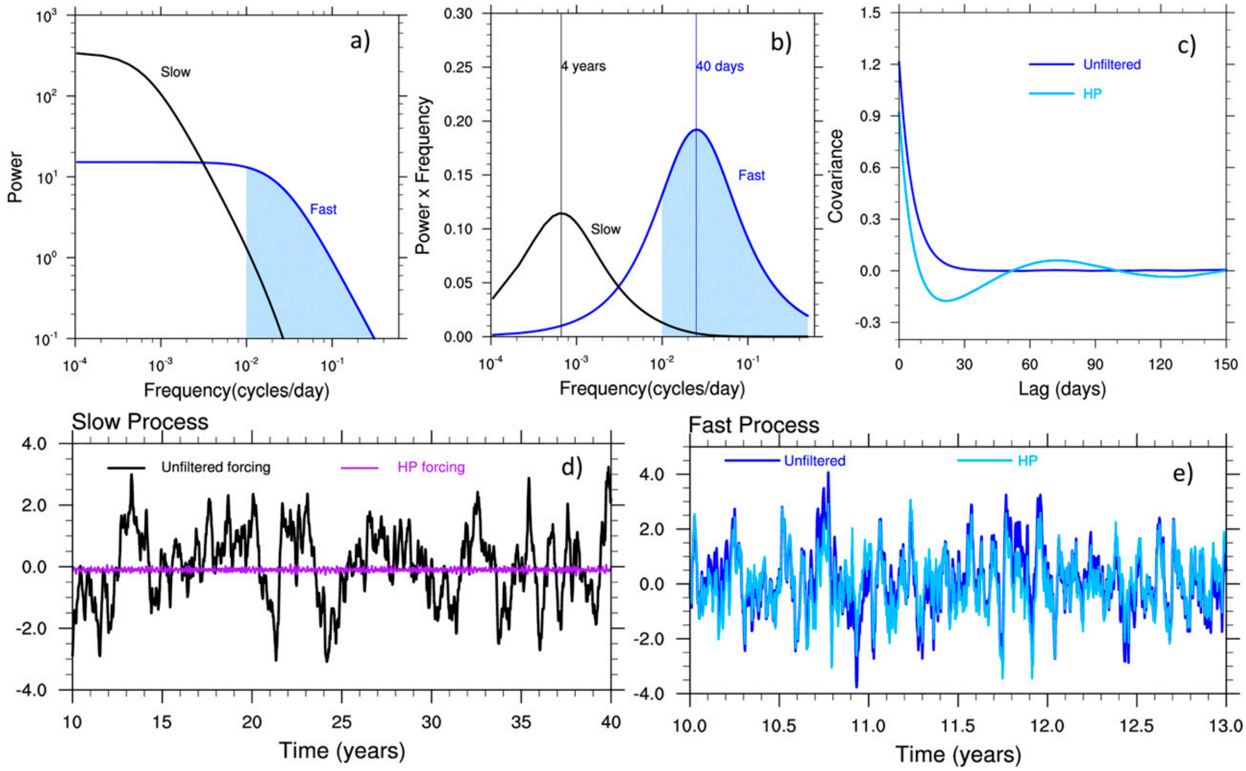

FIG. 1. (a) Spectra (in log-log format) of the slow (x_s; black) and fast (x_f; blue) processes described by Eqs. (1a) and (1b). (b) As in (a), but spectra are shown in variance preserving form. (c) Autocorrelation functions of x_f (dark blue) and its high-pass filtered (HP) component (periods shorter than 100 days; light blue). (d) Sample time series of x_s (black line). The purple line shows the slow process when Eq. (1a) is forced by the HP component of x_f. (e) Sample time series of x_f (dark blue) and its HP component (light blue). The latter is obtained through Fourier filtering by retaining only periods shorter than 100 days [light blue shaded area in (a) and (b)].

the x_s amplitudes are vanishingly small (purple line in Fig. 1d). This occurs despite the sizable amplitude of the high-pass filtered forcing, which is indeed similar to that of the unfiltered forcing (Fig. 1e).

The simple system [Eqs. (1)] is similar to the stochastic climate model used by Frankignoul and Hasselmann (1977) to illustrate, in a univariate framework, how climate variations can arise as an integrated response to "continuous random excitation by short time-scale weather disturbances" (p. 289). Frankignoul and Hasselmann (1977) justified their stochastic model by pointing to the time scale separation of climate and weather processes, allowing the noise forcing spectrum to be approximated as a white noise spectrum at the climatic time scales of interest. Note that in this view, other fast nonlinear tendencies (evaporative cooling, nonlinear advection, etc.) can also be absorbed into the $w(t)$ term in Eq. (1b).

Our very simple model illustrates how, in a linear system, a slow variable with a long correlation scale is effectively forced only by the low-frequency components of a fast variable with a short correlation scale (i.e., with a broadband spectrum). It shows that a relatively small level of low-frequency power of x_f can be sufficient to energize the slow variable, even if the forcing by x_f is independent of x_s (i.e., even if a, b, and λ_f are independent of x_s). This dynamic has been the basis of the linear inverse modeling (LIM) framework of ENSO (Penland and Sardeshmukh 1995), in which the coupled tropical atmosphere–ocean system is approximated as a damped linear dynamical system forced by (in general, spatially varying) white noise. The success of the LIM approach in describing and predicting ENSO (Penland and Sardeshmukh 1995; Newman and Sardeshmukh 2017) is completely consistent with the idea that only the interannual part of the stochastic forcing spectrum matters in generating ENSO variability. However, this idea has never been explicitly validated using observations.

In this study, we use a recently released version of a satellite-based wind vector analysis to investigate the relative role of high-frequency and low-frequency wind variations in the development of ENSO events. We use the data over a 26-yr period (1990–2015), which allows a comprehensive spectral characterization of tropical winds from subdaily to interannual time scales. We will adopt the conceptual framework illustrated in Fig. 1 as a null hypothesis to characterize the stochastic wind forcing of ENSO, viewing it as a red noise process with a correlation scale of a few days. In the system of Eqs. (1) the coefficients a and b are constant and independent of the system state, so the fast forcing acts as ''additive'' noise forcing. Several studies, however, have shown that the amplitude of the fast wind forcing may be modulated by the system state (Yu et al. 2003; Lengaigne et al. 2004; Eisenman et al. 2005; Gebbie et al. 2007; Jin et al. 2007; Levine et al. 2017), so that the wind forcing may also have a state dependent or ''multiplicative'' part. It is possible to assess the relative magnitudes of the additive and multiplicative forcing using our high-time-resolution vector wind dataset. Finally, we revisit the behavior of the tropical Pacific winds in 2014 relative to that in 1997 in terms of their interannual and subseasonal components, instead of focusing only on the different statistics of WWE and EWE events in the two cases as done in some studies (Menkes et al. 2014; Hu and Fedorov 2016). Since the interannual wind variations obviously also contain deterministic components associated with atmosphere–ocean coupling, comparing and contrasting the wind evolution in the interannual and subseasonal frequency bands during 1997 and 2014 provides a clue as to how the different strength of the atmosphere–ocean coupling in the two years might have been another factor in the different behavior of ENSO in those years.

3. Datasets

The primary dataset used in this study is the satellite-based cross-calibrated multiplatform (CCMP) vector wind analysis (Atlas et al. 2011). CCMP uses a variational analysis method to optimally combine satellite retrievals (radiometer wind speeds and scatterometer wind vectors), in situ data from moored buoys (including the TAO/TRITON arrays), and background model fields from the European Centre for Medium-Range Weather Forecasts (ECMWF) to produce a vector wind gridded product at high temporal (6 hourly) and spatial (0.25°) resolution. The version used in this study is CCMP version 2 (V2; Wentz et al. 2015), processed at Remote Sensing Systems, which uses the ERA-Interim reanalysis as background wind field. The most relevant differences compared to CCMP version 1 are described in Ricciardulli et al. (2017). The V2 data are available from 1 January 1988 to the present. Because of gaps prior to 1990, we used the slightly shorter 1 January 1990–31 December 2015 period. A thorough intercomparison of the CCMP product with both satellite and buoy data is underway and will be presented elsewhere. Spurious wind stress curl features have been detected in this dataset at the buoy locations (McGregor et al. 2017); however, we do not expect this to significantly impact our results. Figure 2 provides a reassuring comparison in this regard of the time series of zonal winds during the periods January 1996–December 1999 and January 2014–December 2017 measured at the TAO buoy located at 0°N, 170°W with the exactly collocated CCMP time series in both space and time. The time series of zonal winds derived from the Special Sensor Microwave Imager (SSMI), one of the satellite products incorporated in CCMP, as well as time series from the National Centers for Environmental Prediction (NCEP) Global Data Assimilation System (GDAS) reanalysis, are also included for comparison. The CCMP and SSMI data are highly mutually consistent and in much better agreement with the TAO data than the NCEP-GDAS data during 1996–99 (Fig. 2a). After 2000, the NCEP-GDAS reanalysis started assimilating the scatterometer wind data, and the comparison with the other products is much improved during 2014–17 (Fig. 2b). There are gaps in the TAO data in 2014. Since the TAO data are included in the CCMP variational algorithm, this may raise a concern about the reliability of the CCMP data for 2014. However, the satellite data coverage was excellent in those years. Satellite wind data are considered superior to any reanalysis product (Chelton et al. 2004), and Fig. 2a provides reassurance about the quality of the CCMP product. Indeed, a near-real-time version of CCMP that does not incorporate any buoy data (including TAO), developed at Remote Sensing Systems and available during 2015–17 (Fig. 2b, orange line), agrees well with both satellite and TAO data. Thus, we believe that CCMP is an excellent dataset for our study.

To investigate the variability of the oceanic Kelvin wave field, we used daily sea surface height data from AVISO at 0.25° horizontal resolution in the 1 January 1993–31 December 2016 period (http://www.aviso.oceanobs.com/en/data/products/). We used SSTs from the NOAA Optimum Interpolation (OI) high-resolution dataset, which combines observations from satellite, ships, and buoys on a regular global grid and is available at daily and 0.25° horizontal resolution from September 1988 to the present (Reynolds et al. 2007).

4. Results

a. Time scales of equatorial winds

Spectral analyses of multidecadal time series of surface winds from island sites have provided useful insight

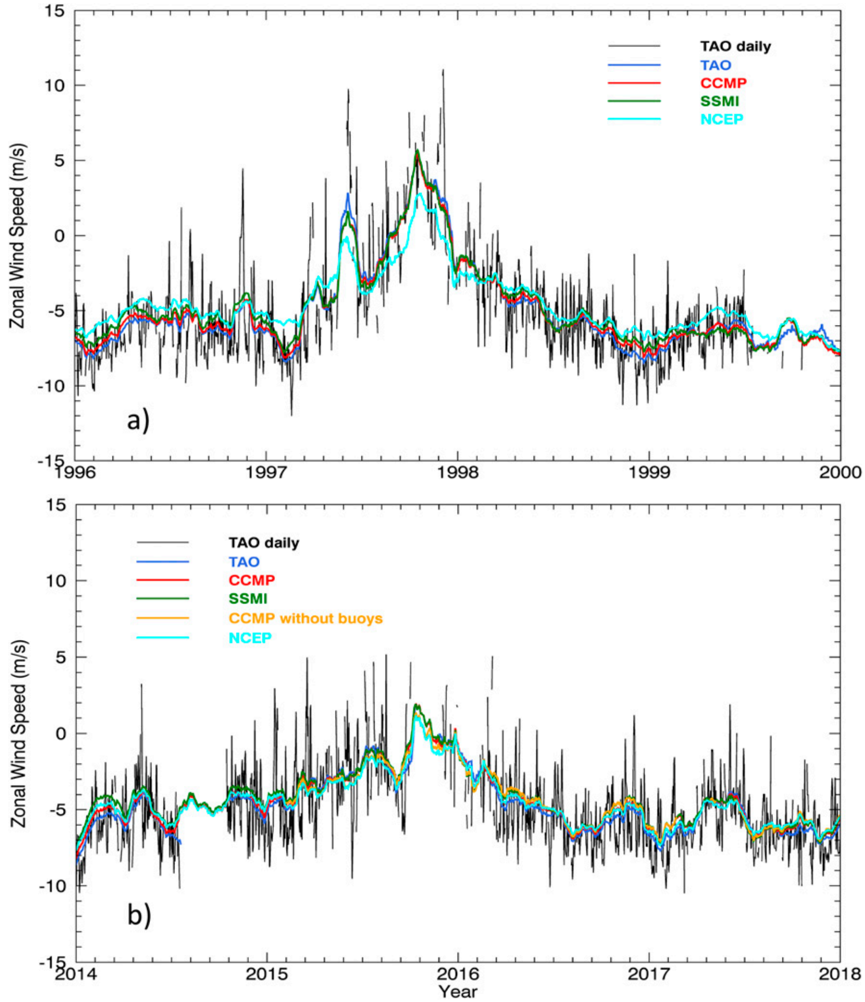

FIG. 2. Comparison of CCMP zonal wind data with TAO data at 170°W and the equator during (a) 1996–2000 and (b) 2014–18. The thin black lines show the daily data measured at the TAO buoy. The 1-month running mean smoothed version of the black line is shown in blue, while the red lines show the 1-month running mean of CCMP data collocated in space and time with the buoy data, when the latter are available. The green lines in both panels show the zonal winds derived from SSMI, and the orange line in (b) shows a near-real-time version of CCMP that does not assimilate the TAO data. The line in teal is the zonal wind derived from the NCEP-GDAS reanalysis.

into the space–time scales of tropical Pacific wind variability (Harrison and Luther 1990). The new CCMP dataset allows a more complete characterization of the wind spectra, whose inconsistencies among previous estimates have been acknowledged (Wittenberg 2004). Following the approach of Harrison and Vecchi (1997), we use the CCMP zonal wind anomalies averaged over the six regions in the equatorial belt (5°S–5°N) shown in Fig. 3. These include the regions considered by Harrison and Vecchi (1997) denoted as W (130°–155°E), C (155°E–180°), and E (180°–155°W), as well as three additional regions in the eastern equatorial Pacific: E1 (155°–130°W), E2 (130°–105°W), and E3 (105°–80°W).

The spectra of the 6-hourly zonal winds in these six regions, presented in a variance preserving form, are shown in Fig. 4. In the western part of the basin (region W) there is modest power in the ENSO band (2–7 years; light blue shading), a sharp annual cycle peak (f_A), and large power at periods shorter than about 100 days. In particular, there is significant power in the 30–90-day band (light pink shading) corresponding to the MJO, as well as at higher frequencies usually associated with WWEs (Lengaigne et al. 2004; Puy et al. 2016). The power in the interannual and subseasonal frequency bands highlighted by light blue and pink shading are more comparable to each other

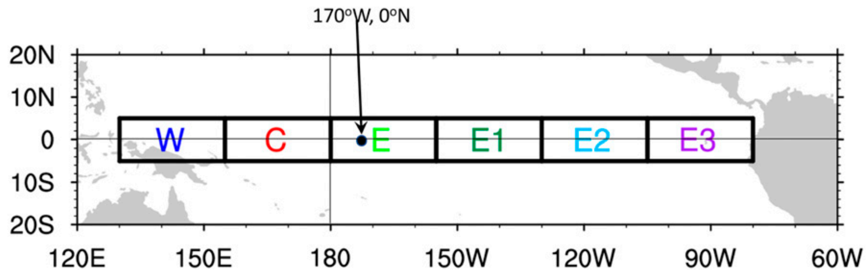

FIG. 3. The six regions used to examine equatorial wind variations. These regions are confined between 5°S and 5°N and span 25° in longitude starting at 130°E (W), 155°E (C), 180° (E), 205°E (E1), 230°E (E2), and 255°E (E3). The W, C, and E regions were introduced by Harrison and Vecchi (1997) to investigate WWE characteristics. We also consider the E1, E2, and E3 regions here to characterize wind variability in the eastern part of the basin. The black dot marks the position of the buoy for which zonal wind time series are considered in Fig. 2.

in regions C and E. These regions overlap with the Niño-4 region, where the westerly wind response to eastern Pacific SST anomalies is strongest, so some of the interannual power in these regions is associated with the deterministic wind response to large-scale SST anomalies. In regions W, C, and E, a spectral peak is also evident around frequency $f_1 = f_A - f_E \approx 2 \times 10^{-3}\,\mathrm{day}^{-1}$ (dotted line on the low-frequency side of the annual peak), where f_A is the annual frequency and f_E is the ENSO frequency, taken here to correspond to a period of ~3.5 years. This spectral peak is close to one of the combination frequencies discussed

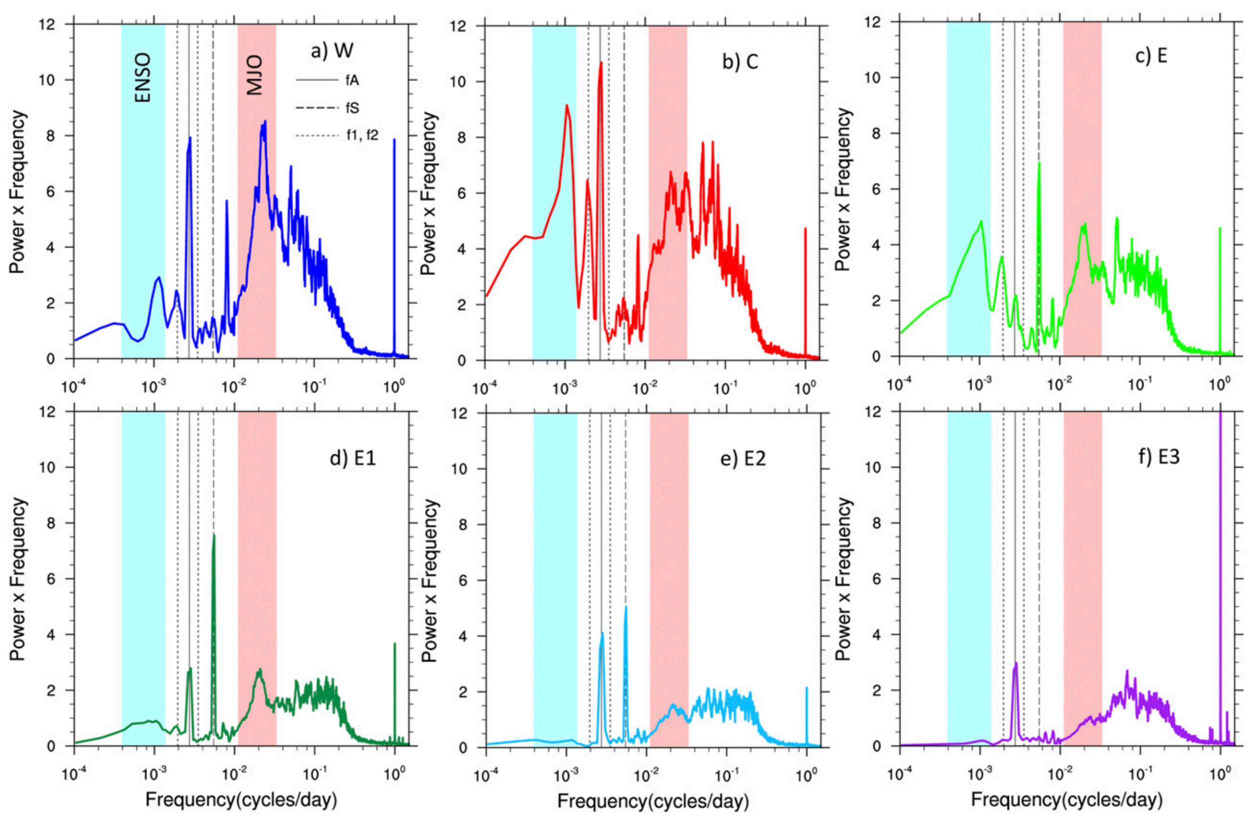

FIG. 4. (a)–(f) Power spectra of zonal winds averaged over the regions shown in Fig. 3. The ENSO (2–7 years) and MJO (30–90 days) bands are highlighted with light blue and pink shading, respectively. The thin solid line indicates the annual cycle (f_A), dashed line the semiannual cycle (f_S), while the two gray dotted lines highlight the combination of $f_1 = f_A - f_E$ and $f_2 = f_A + f_E$ (Stuecker et al. 2013). Power at frequency f_1 can be seen in (a) and especially in (b) and (c).

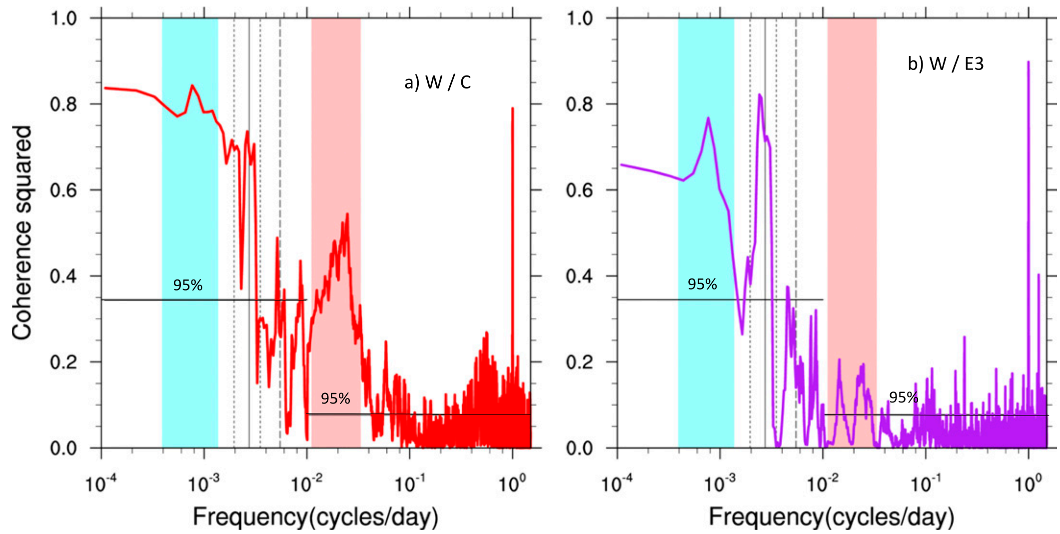

FIG. 5. Coherence squared between the zonal wind variations in region W and those in (a) region C and (b) region E3. Different levels of smoothing of the cospectral estimates have been applied for frequencies lower or higher than 10^{-2} day^{-1} (100 days), with a fewer spectral bins averaged at lower frequencies. As a result, the 95% significance level, estimated according to Julian (1975) is different in the two frequency bands.

by Stuecker et al. (2013). The second combination mode at frequency $f_2 = f_A + f_E$, (dotted line on the high-frequency side of the annual peak) is, interestingly, not evident in this dataset. Annual and diurnal peaks are evident in all six regions, with the semiannual peaks (f_S) dominating in regions E, E1, and E2 (180°–105°W), in agreement with Goldenberg and O'Brien (1981). In the eastern part of the basin (regions E1, E2, and E3) there is relatively less power at all frequencies, especially in the interannual band.

One of the processes by which anomalous equatorial winds influence ENSO is through excitation of oceanic equatorial Kelvin waves. The spatial coherence of the surface wind forcing likely plays an important role in forcing such Kelvin waves that can propagate to the eastern ocean boundary with significant amplitude. If winds at different longitudes reinforce the oceanic signal as it propagates eastward, it can be expected to grow in strength, as shown by Capotondi et al. (2003) for extra-equatorial Rossby waves. Here we examine the spatial coherence of the equatorial zonal winds at different frequencies through a cospectral analysis of the winds in the different regions. Cospectral analysis estimates the degree of ''correlation'' between two time series as a function of frequency and provides both amplitude (squared coherence) and phase information. For example, time series at different longitudes with a statistically significant squared coherence and a difference in phase represent a zonally propagating signal. On the other hand, statistically significant coherent signals with a 0° or 180° phase difference indicate standing signals that are either in phase or opposite phase at the two longitudes. Cospectral analysis can thus be a powerful tool for examining the propagation of signals in specific frequency bands and estimating their phase speed (Capotondi and Alexander 2001). Here, we are primarily interested in understanding the degree of coherence at different longitudes for either propagating or standing signals.

Figure 5 shows the squared coherence of the zonal wind variations in region W with those in regions C and E3. Although region C is just to the east of region W and has large power at subseasonal frequencies, the squared coherence in that frequency range (except at MJO frequencies) is significantly lower than that at interannual frequencies. This is consistent with the limited 30° longitude zonal extent of the wind anomalies associated with WWEs (Seiki and Takayabu 2007; Puy et al. 2016). The relatively low squared coherence between regions W and C at submonthly frequencies may limit the ability of wind variations at those frequencies to excite and sustain a vigorous Kelvin wave field that can intensify and propagate all the way to the eastern ocean boundary, as further discussed in section 3c. Nonetheless, the wind variations in region W at MJO frequencies remain significantly coherent with those in regions E1 and E2 (not shown). Indeed, the variations in E3 are coherent with those in W also at interannual, annual, and diurnal time scales (Fig. 5b).

b. *Interplay of subseasonal and interannual wind variations*

An interesting aspect of the spectra in Figs. 4a–c is the spectral gap between the interannual and intraseasonal bands, also noted by Harrison and Luther (1990) in their analysis of vector winds at a group of tropical islands. The gap suggests a natural way to separate the variability in the two bands. To that end, we first removed the annual cycle by subtracting, at each time, the mean calendar time value over the total duration of the record. We then used Fourier filtering to separate the low-frequency (LF) variations (periods longer than 250 days) from the high-frequency (HF) variations (periods between 250 days and 5 days). Since the LF component has larger power at periods longer than one year, we will also refer to it as the interannual component. We will similarly refer to the HF component as the subseasonal component, since most of the power in the HF band is at periods shorter than three months.

The resulting time series in regions W, C, and E, reconstructed as the superposition of the LF and HF wind components, are shown in Fig. 6. It is clear that the commonly used definitions of WWEs and EWEs based on amplitude and duration thresholds are strongly influenced by LF variations. The latter include the zonal wind anomalies associated with the Bjerknes feedback. As such, definitions of WWEs based on departures from the annual cycle rather than from the interannual variations may confound the WWE statistics. In particular, the apparently larger probabilities of strong WWEs during El Niño and strong EWEs during La Niña may partly be an artifact of the WWE and EWE definitions. Hence, we explicitly separate the HF and LF variations and examine their separate connections with ENSO.

As mentioned earlier, the canonical view of stochastic wind forcing of ENSO involves the excitation of oceanic equatorial Kelvin waves that deepen the thermocline in the eastern Pacific, initiating the Bjerknes feedback. WWEs are also considered important in displacing the eastern edge of the western Pacific warm pool farther eastward, and the resulting warming of the central Pacific has been viewed as conducive to increasing the amplitude and eastward displacement of the WWEs themselves. The 1997/98 El Niño event is often used to illustrate these processes, as shown in Fig. 7. Starting around the end of 1996, pulses of anomalous westerly winds developed in the western Pacific, intensified and propagated eastward during 1997, and slowly decayed in the first part of 1998 after the peak of the El Niño event (Fig. 7a). The evolution of the anomalous westerlies was accompanied by eastward propagating positive SSH anomalies (corresponding to a deeper thermocline) that

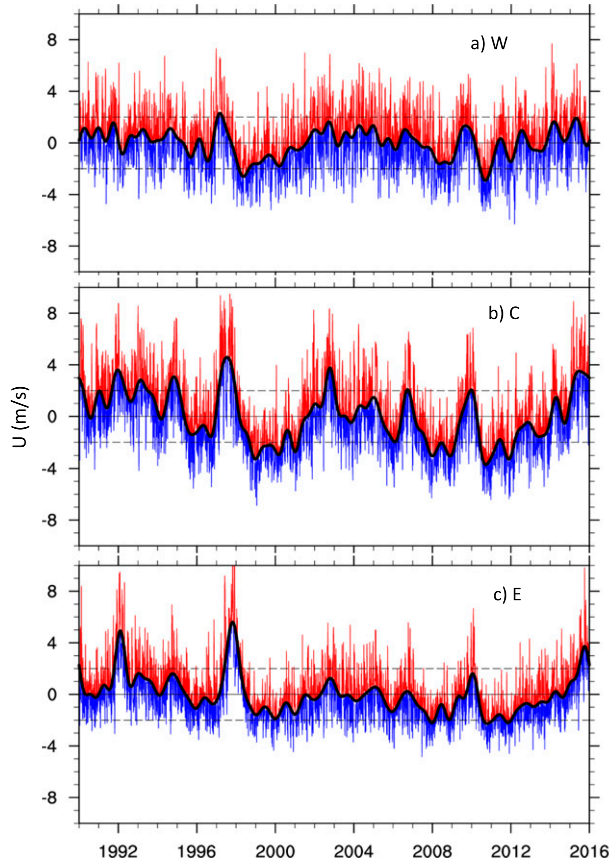

FIG. 6. Time series of 10-m zonal wind ($m\,s^{-1}$) in regions (a) W, (b) C, and (c) E. The time series have been created by first removing the annual cycle, then separating, through Fourier filtering, the LF (periods longer than 250 days; thick black line) from the HF (periods in the 5–250 days range) signals, and then reconstructing the time series as the sum of LF and HF. The HF signal is further separated into positive (red) and negative (blue) components. Thin dashed lines indicate $\pm 2\,m\,s^{-1}$ values, which have been used as an amplitude threshold in the definition of the WWEs (Harrison and Vecchi 1997).

achieved their largest amplitude east of ~135°W in the fall and winter of 1997 (Fig. 7b). The development of the SSH anomalies was concurrent with the development of SST anomalies east of the date line. The pulses of westerly winds seen in Fig. 7a have been considered essential to the development of this strongest El Niño on record in the eastern equatorial Pacific (McPhaden 1999; Yu et al. 2003).

However, when the equatorial wind evolution in Fig. 7a is decomposed into its LF and HF components (Fig. 8, showing only the evolution during 1997, for clarity) it is clear that the LF component was the key player in the wind evolution during this time period. In particular, the intensification and eastward propagation of the WWEs inferred from the evolution of the total

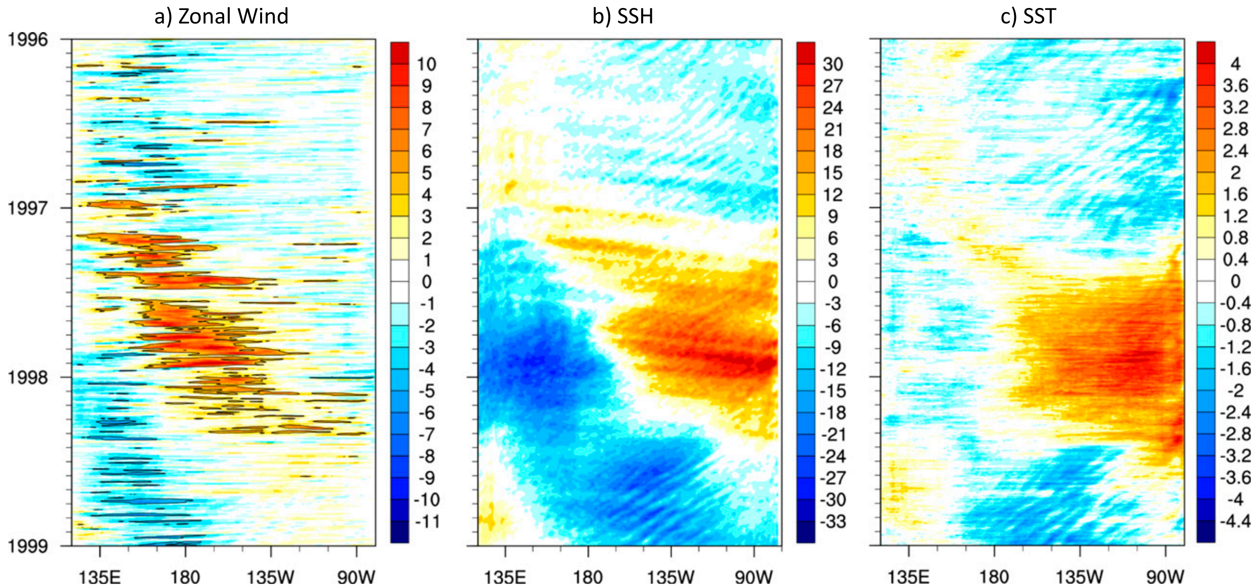

FIG. 7. Equatorial evolution of (a) zonal wind anomalies ($m\,s^{-1}$), (b) SSH anomaly (cm), and (c) SST anomaly (°C) during 1996–99 as a function of longitude (horizontal axis) and time (vertical axis), with time increasing downward.

wind anomalies (Figs. 7a and 8a), emphasized in many studies (Yu et al. 2003; Eisenman et al. 2005, among others), were primarily associated with the LF part of the wind anomalies. The HF variations (Fig. 8c) had a relatively short fetch, consistent with the low squared coherence of the HF winds between regions W and C in Fig. 5. They were also associated with rapidly alternating positive and negative anomalies, resulting in a sequence

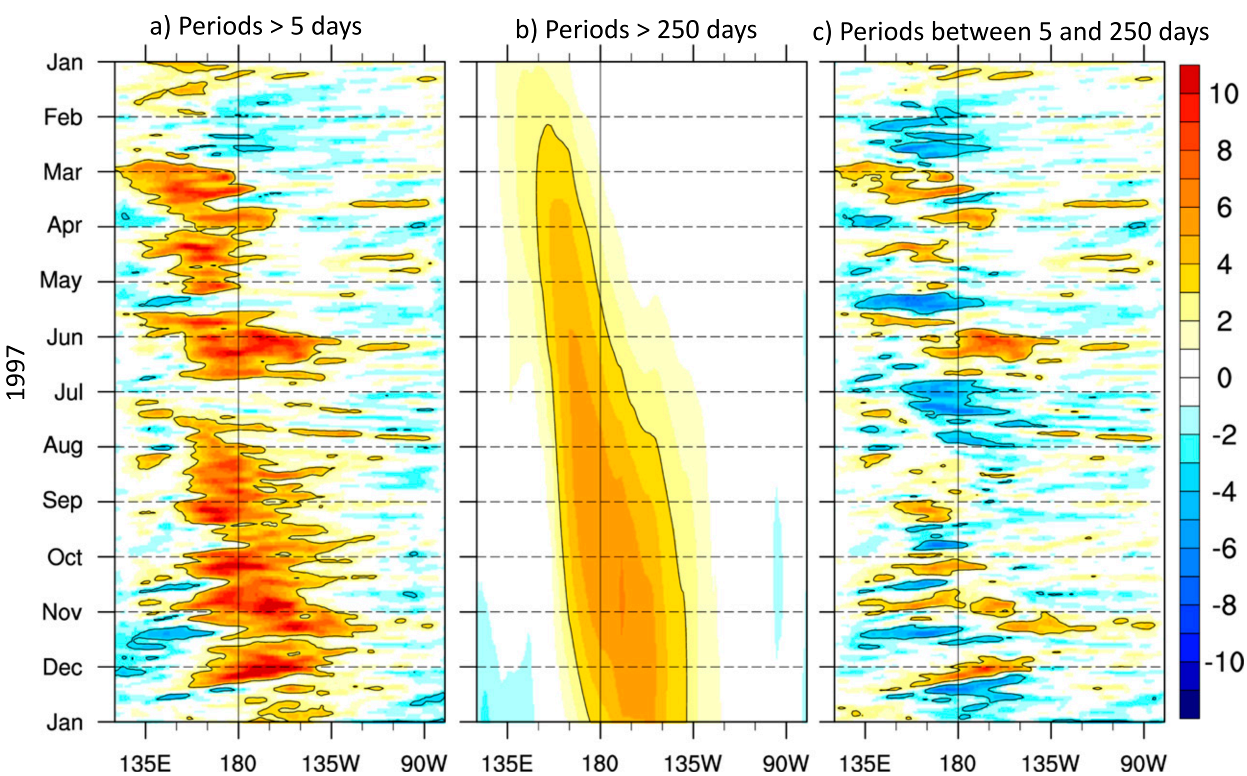

FIG. 8. Equatorial evolution of zonal wind anomalies ($m\,s^{-1}$) during 1997 as a function of longitude (horizontal axis) and time (vertical axis), with time increasing downward. (a) Periods longer than 5 days. (b) Periods longer than 250 days (LF). (c) Periods between 5 and 250 days (HF). Fourier filtering has been used to separate the different frequency bands. Values of $\pm 3\,m\,s^{-1}$ are contoured. The date line is marked for reference by the thin solid black line.

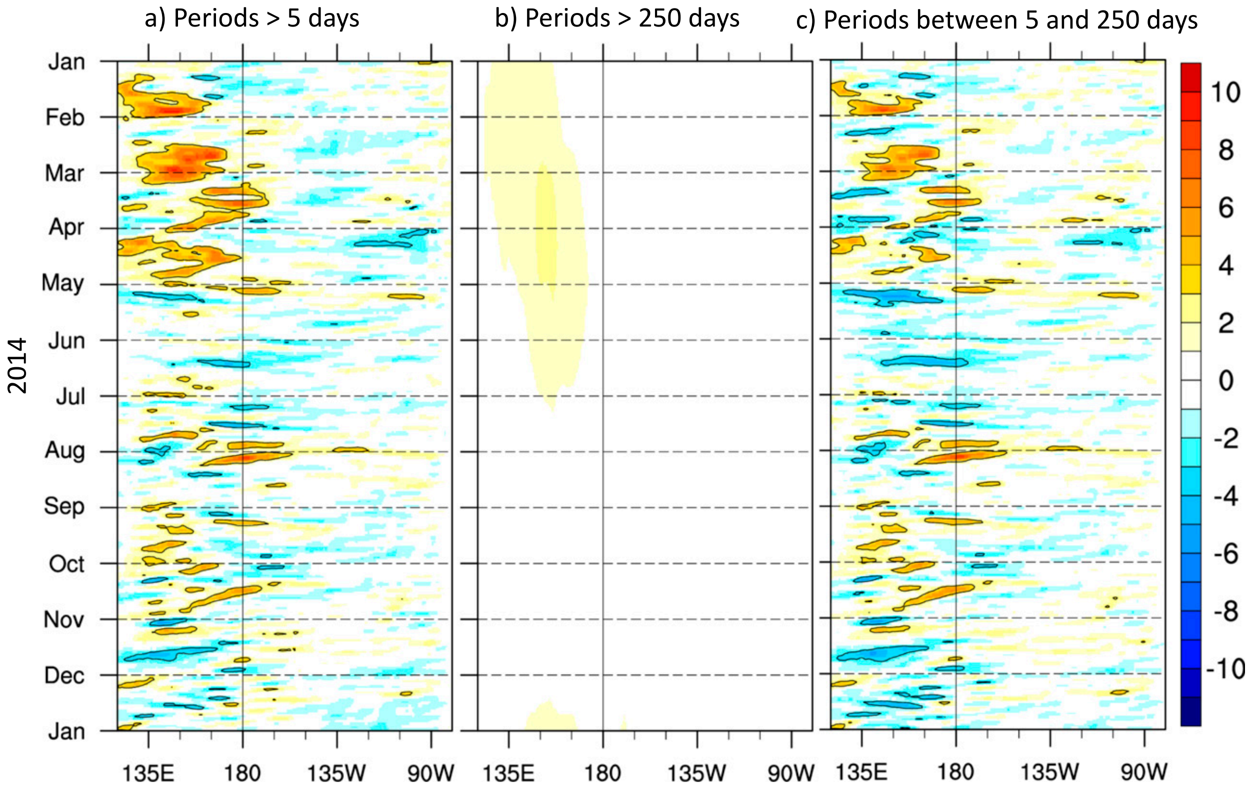

FIG. 9. As in Fig. 8, but for 2014.

of downwelling and upwelling Kelvin waves, whose net contribution to the thermocline variations in the eastern Pacific may be questionable.

It is interesting to compare and contrast the wind evolution during 1997 with that during 2014 (Fig. 9). Similar to 1997, westerly wind pulses also occurred during January–April 2014, leading some researchers to anticipate a big El Niño event. However, that big event did not come to pass, with only weak SST anomalies observed in the central and eastern equatorial Pacific later in the year. The lack of WWEs in the summer months of 2014 (Menkes et al. 2014) and the occurrence instead of EWEs in May and June (Figs. 9a,c; Hu and Fedorov 2016; Levine and McPhaden 2016) have been suggested as possibly important in halting the development of this El Niño event. When viewed in terms of HF and LF wind variations, Figs. 8 and 9 show that the main difference between the two years was the missed development of a strong LF wind component in 2014 (Fig. 9b), in stark contrast to the strong development of LF winds in early 1997 (Fig. 8b). This suggests that differences in large-scale conditions, perhaps including extratropical Pacific influences, may have been responsible for weaker air–sea coupling in 2014, leading to a dramatically different evolution of the equatorial Pacific in 2014 relative to 1997.

c. *Which time scales of wind variability are most effective in triggering ENSO?*

The effectiveness of HF wind variations in triggering ENSO events has been questioned in several studies (Roulston and Neelin 2000; Eisenman et al. 2005; Gebbie et al. 2007; Lopez et al. 2013; Zavala-Garay et al. 2008). Most of these studies were carried out in modeling contexts, by considering an ocean model's response to atmospheric noise in different frequency bands (Roulston and Neelin 2000), by testing the influence of different WWE parameterizations on model ENSO events (Eisenman et al. 2005; Gebbie et al. 2007), or by examining the influence of atmospheric noise in hybrid ENSO models (Zavala-Garay et al. 2008). Here we revisit this issue using different satellite-based observational products. Figure 10a compares the spectrum of zonal wind over the western/central Pacific (5°S–5°N, 130°E–155°W, spanning regions W, C, and E, hereafter the WP region) with the spectra of SSTs over the eastern equatorial Pacific (5°S–5°N, 155°–80°W, spanning regions E1, E2, and E3) and SSH across the basin (5°S–5°N, 130°E–80°W). All time series are daily averages and normalized to unit standard deviation, and the spectra are displayed in variance preserving form. While the wind spectrum has

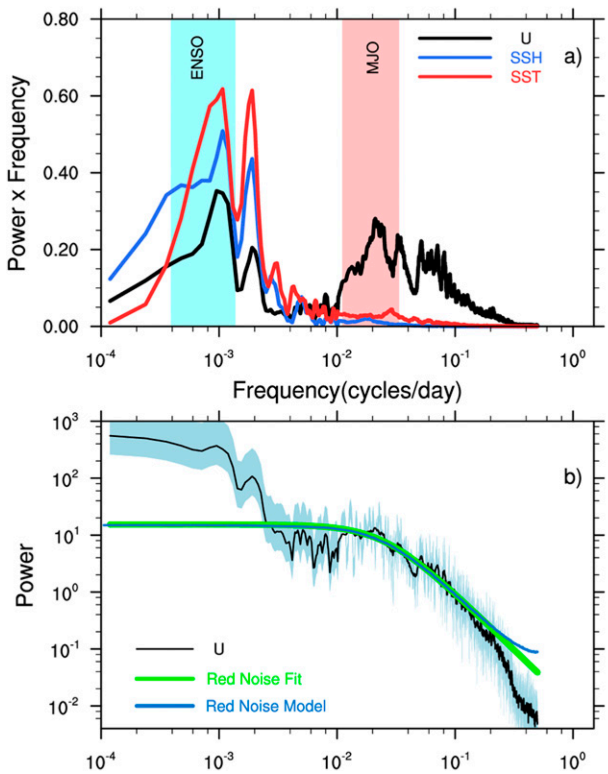

FIG. 10. (a) Spectra of normalized daily time series of zonal winds (black), SSH (blue) and SST (red). Each time series has been normalized by its standard deviation. The zonal winds are averaged in the region 5°S–5°N, 130°E–155°W, SSH is averaged over 5°S–5°N, 130°E–80°W, and SST is averaged over 155°–80°W. Spectra are displayed in variance preserving form. The ENSO (2–7 years) and MJO (30–90 days) bands are highlighted with light blue and pink shading, respectively. (b) The black curve shows the log-log representation of the same wind spectrum shown in (a) with its 95% confidence interval (light blue shading). The green curve shows the spectrum of a red noise process fitted to the HF ($f > 10^{-2}$ day^{-1}) part of the wind spectrum using a nonlinear least squares fitting, while the blue line shows the average spectrum of the 300 26-yr segments of 7800 years of a red noise model output constructed with the parameters of the nonlinear fit.

comparable power in both the LF and HF bands, as already noted, most of the SST and SSH power is at frequencies lower than (500 days)$^{-1}$, suggesting that the oceanic fields respond preferentially to wind variations in the LF range, consistent with our conceptual framework in Fig. 1 as well as with modeling studies (e.g., Roulston and Neelin 2000). Large dynamical nonlinearities could ''rectify'' the HF onto the LF variations. However, the importance of such nonlinearities has never been definitively established in observational contexts.

Since HF wind variations are believed to influence SSTs in the eastern equatorial Pacific through oceanic Kelvin wave excitation, we examine the equatorial evolution of SSH anomalies in the same HF band. This comparison is shown in Fig. 11 for 1997 and 2014. The SSH anomalies exhibit eastward propagating signals with phase speeds of ~2.6 m s^{-1}, as estimated from the slope of the black dotted line in Fig. 11a. This value is consistent with typical phase speeds for first baroclinic mode equatorial Kelvin waves (Gill 1982). The upwelling and downwelling Kelvin wave signals can be related to easterly and westerly pulses of wind anomalies (as indicated by the red and blue hatched patches of HF wind anomalies larger than 3 m s^{-1} in absolute value), respectively, confirming the ability of HF wind variations to excite oceanic Kelvin waves at the same frequencies. The comparison of westerly and easterly wind pulses with the Kelvin wave field shows how the limited zonal extent and duration of these pulses, which results in reduced zonal coherence (section 3a), can occasionally limit their ability to trigger Kelvin waves that propagate with sizeable amplitude to the eastern ocean boundary. This can be seen, for example, in early May 1997, when the negative SSH anomaly west of the date line, concurrent with an easterly wind pulse, is halted by the positive SSH anomalies associated with a subsequent westerly wind burst occurring to the east of the initial easterly event. A similar interplay of westerly and easterly wind pulses can also be seen during September–October 1997. It is interesting to compare the HF SSH evolution during 1997 with that during 2014. In both cases, a sequence of upwelling and downwelling Kelvin waves can be seen. The HF easterly wind pulses and associated upwelling Kelvin waves seen in the summer of 2014 do not stand out as unusually large, as signals of comparable magnitude can be seen also in 1997. As noted in section 4b, the lack of strong LF westerlies in 2014 was the main difference with 1997.

Figure 12 shows that the LF SSH variations have much larger amplitudes than the HF SSH variations. In fact, comparing the zonal equatorial profiles of SSH variance in the LF and HF bands shows that the HF variance accounts for only about 12% of the total SSH variance in general (Fig. 13). Similarly, HF SST anomalies are much weaker than LF anomalies (not shown).

In summary, while our analysis confirms the existence of HF Kelvin waves excited by HF wind anomalies, they represent only a small part of the total SSH anomalies, and cannot be expected to contribute substantially to SST variations in the eastern equatorial Pacific. Our conclusion is in agreement with that of Zavala-Garay et al. (2008), who showed that the subseasonal Kelvin wave field accounted for a very small part of ENSO evolution in their hybrid coupled models.

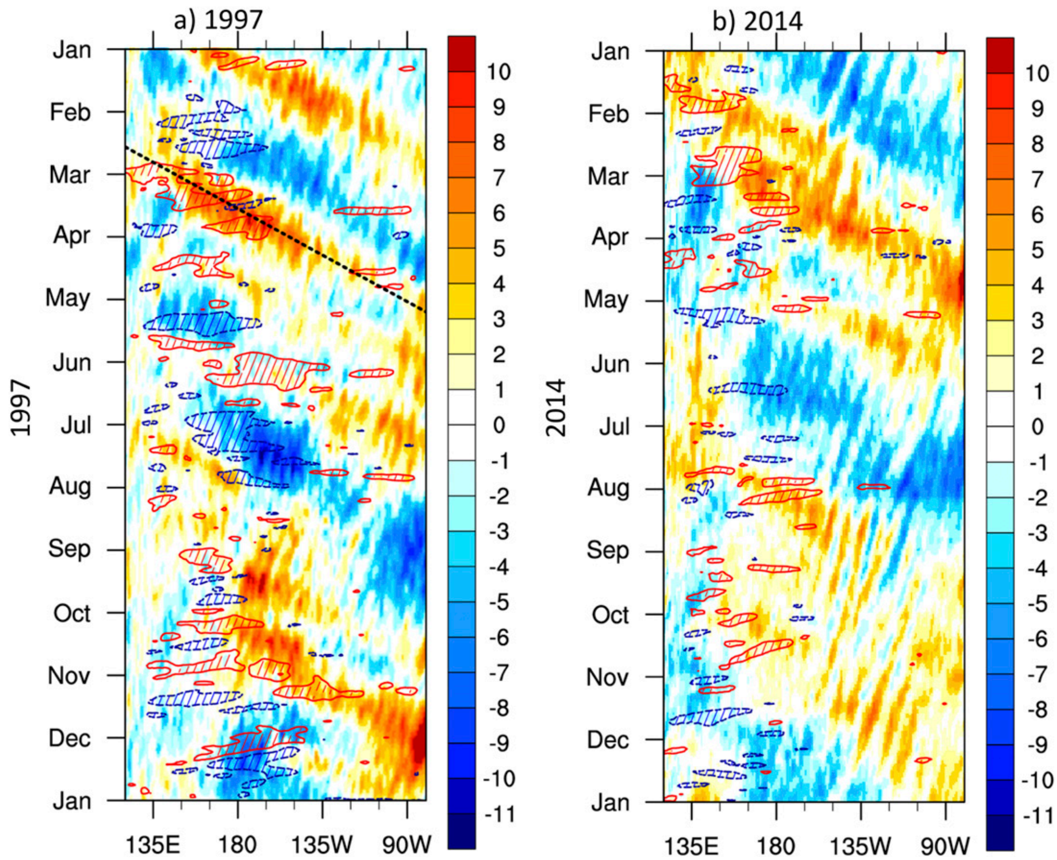

FIG. 11. Illustration of the relationship between intraseasonal (5–250 days) equatorial oceanic Kelvin waves (shading) and intraseasonal wind variations (hatched areas) during (a) 1997 and (b) 2014. SSH (cm) is shown with shading. HF winds larger than $3\,\mathrm{m\,s^{-1}}$ in absolute value are indicated by the red hatching for positive values (westerlies) and blue hatching for negative values (easterlies). The black dotted line in (a) highlights the eastward propagation of the oceanic signals and corresponds to a phase speed of $2.6\,\mathrm{m\,s^{-1}}$.

d. Where does "climate noise" come from?

Roulston and Neelin (2000) suggested that the stochastic wind forcing of ENSO may originate outside the tropical Pacific, while other investigators (Eisenman et al. 2005) have viewed the LF component of WWEs as resulting from the SST modulation of the WWEs. Other nonlinear processes can also produce LF noise components through rectification of HF wind variations (Kessler and Kleeman 2000; Rong et al. 2011). However, as stressed in section 2, fast forcing with a correlation time scale of a few days has power at both high and low frequencies. To estimate the low-frequency power level of the zonal winds, a power spectrum of the form shown in Fig. 1a for the fast process x_f

$$P_f = (b/2\pi)^2/(f^2 + r^2) \tag{2}$$

was fitted to the HF part (periods shorter than 100 days) of the zonal wind spectrum in Fig. 10b. In Eq. (2), f is frequency, $r = (2\pi\tau_f)^{-1}$, and b is the amplitude of the white noise in Eq. (1b). For $f \ll r$ (time scales much longer than the correlation time scale of the fast process), P_f asymptotes to $(b/2\pi r)^2$, while for $f \gg r$ it decays as $1/f^2$. The red noise spectrum was estimated using a least squares nonlinear fit, yielding a correlation time scale $\tau_f = 6.4$ days. Equation (2) provides an overall excellent fit to the high-frequency part of the observed wind spectrum, although the observed spectrum decays faster than $1/f^2$ at time scales shorter than ~8 days. The reason for this discrepancy is likely associated with the multivariate nature of the observed wind variations, which is ignored in the univariate approximation in Eq. (2), as discussed in Sardeshmukh and Penland (2015). Our hypothesis is that the subseasonal part of the spectrum in Fig. 10b can be viewed as the high-frequency tail of a red noise process characterized by a correlation time scale much shorter than the time scales of ENSO, in analogy with our conceptual framework in

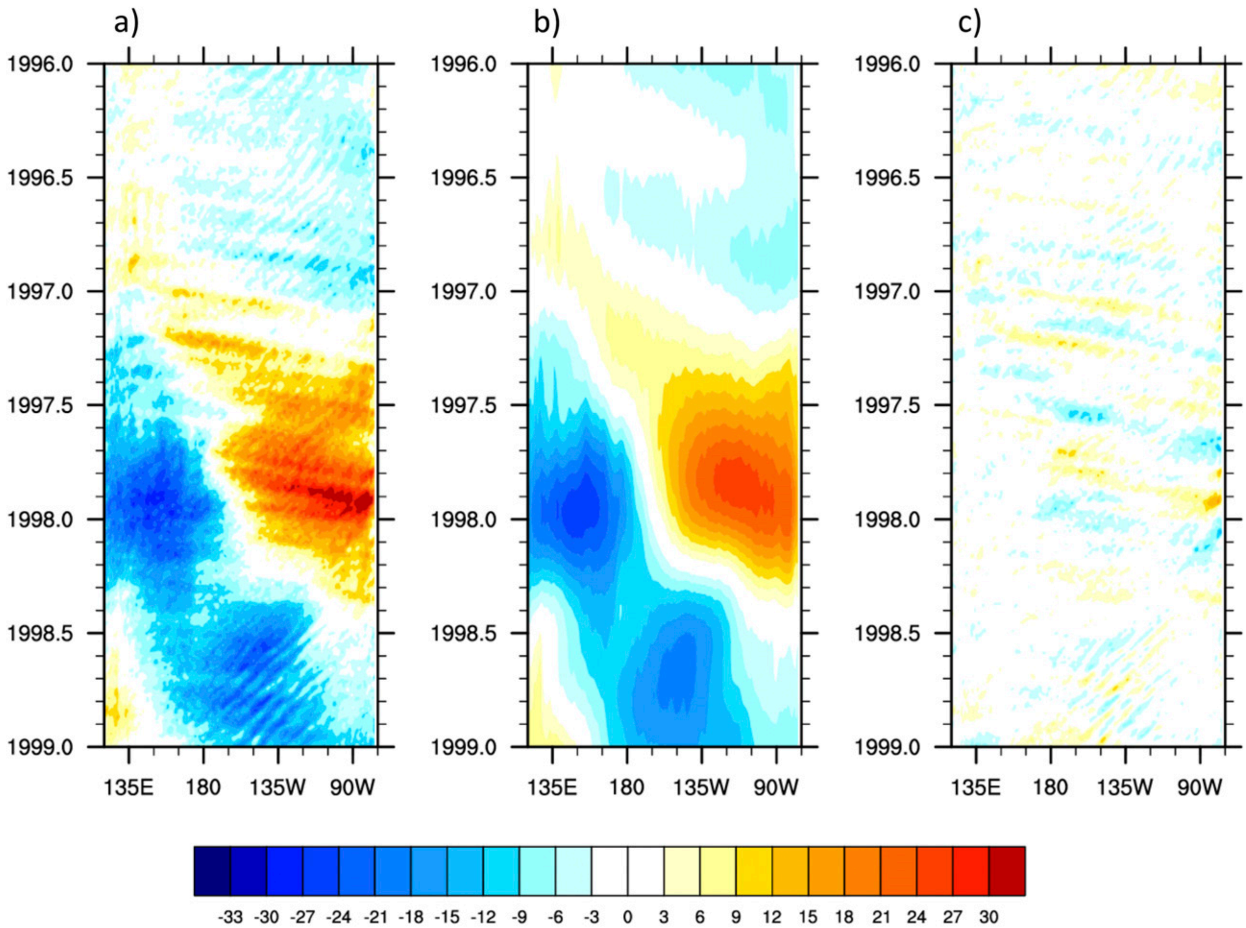

FIG. 12. Evolution of equatorial SSH anomalies (cm) as a function of longitude and time during 1996–99. Time increases downward. (a) Total field (periods longer than 5 days). (b) LF component (periods longer than 250 days). (c) HF component (periods shorter than 250 days and longer than 5 days).

Fig. 1 and with the early stochastic modeling studies of Frankignoul and Hasselmann (1977). In our view, the reddening of the noise spectrum is associated with correlation time scales that are typical of tropical subseasonal processes like the MJO, and does not require "ocean memory" outside the tropical Pacific as hypothesized by Roulston and Neelin (2000). The use of monthly mean data by Roulston and Neelin (2000) may also have limited the characterization of the noise and accurate estimation of so-called ocean memory in their study.

Our hypothesis that the stochastic wind forcing of ENSO is the flat low-frequency tail of a red noise wind spectrum is supported by the spectra for individual years in our study period, shown in Fig. 14a. The yearly spectra also have a similar character to that described by Eq. (2), with a tendency to flatten at periods longer than approximately 50–60 days. This further supports the view that stochastic forcing cannot be considered as purely high-frequency wind fluctuations, but rather as a short-correlation Markov process that spans a broad range of frequencies including those in the ENSO band.

e. Is stochastic wind forcing dependent upon the ENSO state?

Several studies have investigated the connection between the frequency and strength of WWEs and SST anomalies (e.g., Yu et al. 2003; Eisenman et al. 2005; Tziperman and Yu 2007; Gebbie et al. 2007). The basic premise of these studies is that WWEs are more likely to occur over warm waters. As the eastern edge of the warm pool extends eastward during an El Niño development, the WWEs also tend to occur farther east with increasing strength. The above studies used definitions of WWEs as departures from the seasonal cycle, so that, as implied in Fig. 6, more WWEs were likely to be identified during El Niño events partly as a result of the superposition on the LF winds forced by the SST

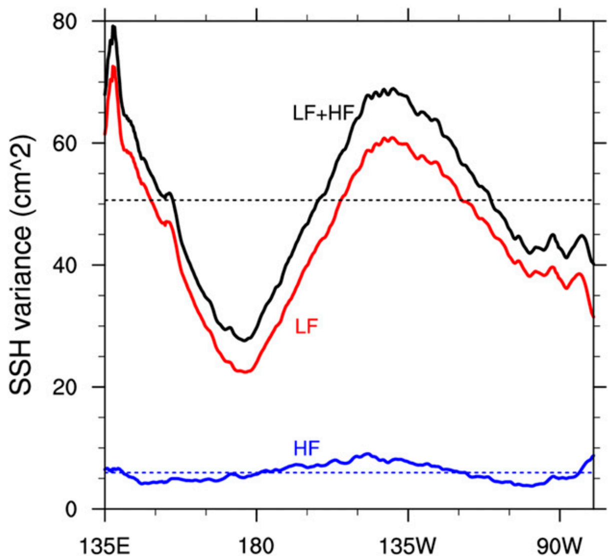

FIG. 13. Equatorial profiles of the SSH variance, computed over the full duration of the record, as a function of longitude. The black curve is for SSH variations at periods longer than 5 days, the red curve is for the LF (periods longer than 250 days) component, and blue is for the HF (periods shorter than 250 days and longer than 5 days) component. The average variance of the HF signal (dashed blue line) is only about 12% of the average variance of the total signal (dashed black line).

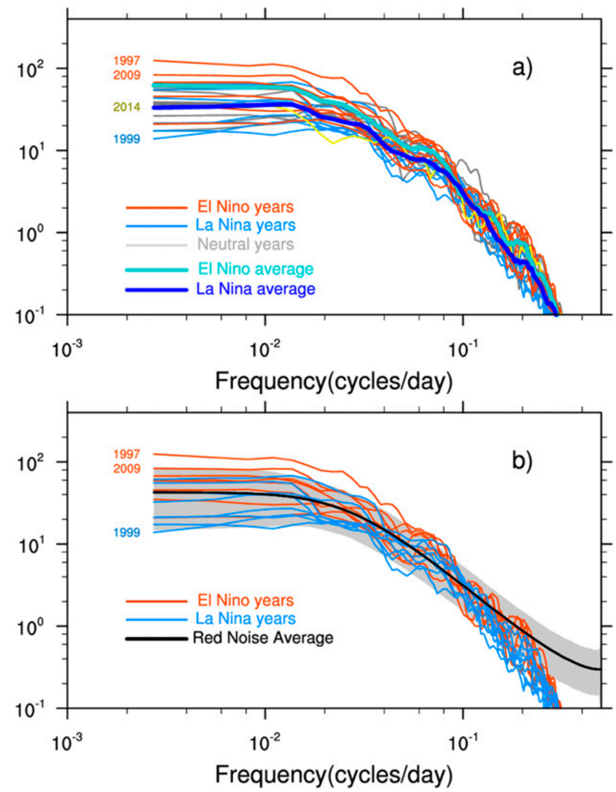

FIG. 14. (a) Comparison of zonal wind spectra during El Niño years (thin orange lines), La Niña years (light blue lines), and neutral years (gray lines). The thick teal and blue lines are the average spectra for El Niño and La Niña years. The spectrum for 2014 is shown in yellow for comparison with 1997. (b) Spectra of wind anomalies for El Niño and La Niña years are compared with the average yearly spectrum obtained from the red noise model. Gray shading highlights the 2.5 and 97.5 percentile values of the yearly spectral estimates from the red noise model (see text for details).

anomalies. Here we attempt to remove this effect and explicitly consider the dependence of the HF zonal wind variations on the SST anomalies. To this end, we constructed an index of HF wind activity by squaring the daily means of the HF time series, computing a 360-day running average, and then taking the square root of the resulting time series. These HF indices for regions W, C, and E are compared with the Niño-3.4 SST anomaly index in Figs. 15a–c, respectively. In all three regions, but especially in regions C and E, the HF index corresponds well with ENSO, with a tendency for the HF winds to lead ENSO. This is quantified by correlation analysis. In region W, the correlation between the HF index and the Niño-3.4 index is 0.50, with the HF index leading by about 10 months. The correlations increase to 0.70 and 0.72 in regions C and E, with the HF index leading by 3 months and 1 month, respectively. The correlation in region W is only significant at the 80% level based on a one-tailed Student's *t* test with 7 degrees of freedom, while the correlations in regions C and E are significant at the 95% level. The number of degrees of freedom used in these significance tests were based on the effective sample size (Trenberth 1984), approximately equal to the number of ENSO cycles over the length of the record.

These correlation statistics are consistent with the results of Kug et al. (2008) based on daily wind data from the NCEP–NCAR reanalysis (Kalnay et al. 1996). Kug et al. (2008) suggested that HF wind anomalies in the western Pacific act as El Niño triggers, while the quasi-simultaneous correlation in region E suggests a dependence of the atmospheric noise upon the ENSO state. This state dependence may be better gauged by examining the simultaneous relationship between the HF index in each region and the SST anomaly time series in that same region. The SST time series in regions W, C, and E are indicated by the gray dotted lines in each panel of Fig. 15. The HF wind fluctuations are almost uncorrelated with the local SST fluctuations in region W, but not in regions C and E. In these regions, however, the local SSTs are highly correlated with the Niño-3.4 index itself, making it difficult to distinguish between cause and response. In region C, the local SST time series tracks the Niño-3.4 index more closely after

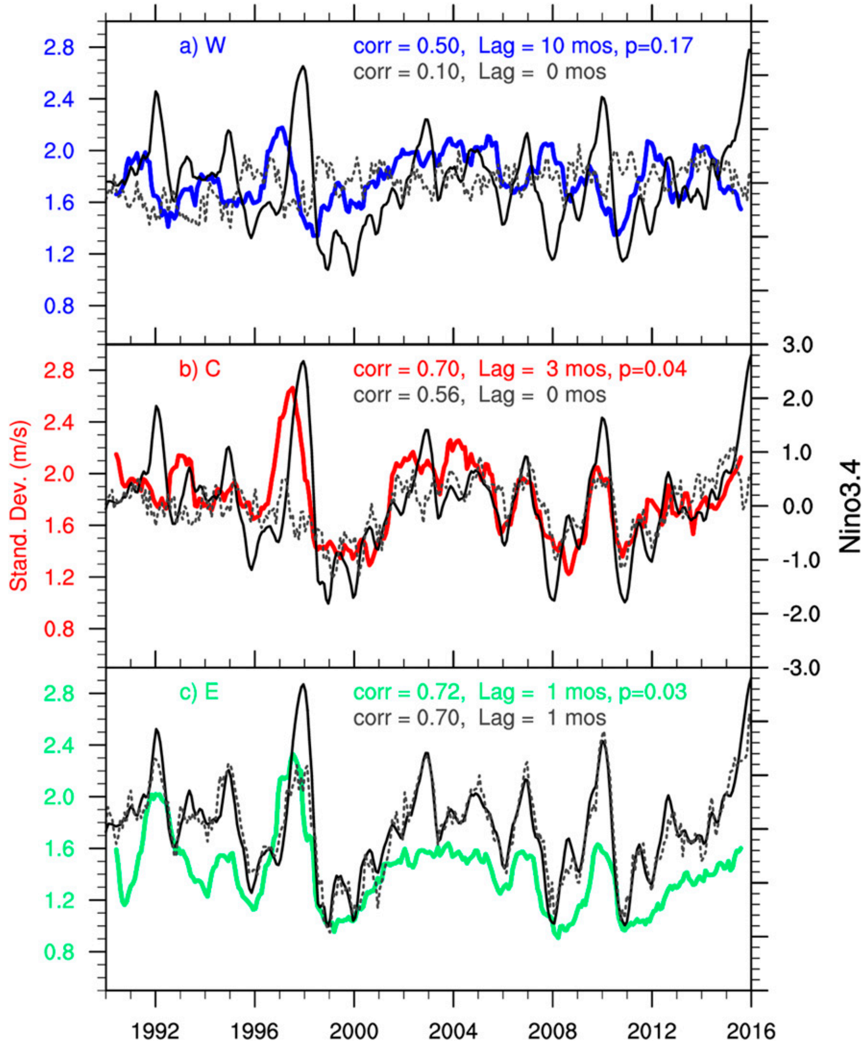

FIG. 15. Indices of HF zonal wind activity in regions (a) W, (b) C, and (c) E. Please see text for details about the index computation. The HF index in each region (colored line; left axis) is compared with the Niño-3.4 index (black line; right axis) and with the SST anomaly time series in the same region (gray dotted line; right axis). The maximum correlations between the wind index and the Niño-3.4 are 0.50, 0.70, and 0.72 in regions W, C, and E, respectively, with the winds leading by 10 months in region W, 3 months in region C, and 1 month in region E. The p values from a Student's t distribution indicate that the correlation coefficients are statistically significant at the 80% level in region W and 95% in regions C and E for a one-tailed significance test. The maximum correlations and associated lags of the HF indices with the local SST anomalies are shown in gray.

1998, when most of the El Niño events had large SST anomalies in the central Pacific, whereas the strong 1997/98 eastern Pacific event had a relatively small positive SST signature in region C. The presence of a large HF wind signal in regions W and C, preceding the 1997/98 event, which was apparently only weakly related to the local SST anomalies, suggests that for this event a significant fraction of the HF wind variations in these regions acted as ENSO forcing rather than response.

An interesting result in Fig. 15 is that the HF forcing (including positive and negative fluctuations) is higher during El Niño than La Niña events. This apparently disagrees with Chiodi and Harrison (2015), who related La Niña events to the occurrence of EWEs in the preceding months (April–December). The discrepancy may partly be due to the definition of EWEs used by Chiodi and Harrison (2015) based on wind stress anomalies relative to the annual cycle, rather than departures from the LF component. As seen in Fig. 6, if the LF wind components are not removed, the stronger LF easterly winds during La Niña events can contribute to an erroneous detection of enhanced EWE activity.

A similar dependence of the noise level on the ENSO state is also evident in the spectra for El Niño/La Niña years versus neutral years in Fig. 14a. For this purpose, we identified eight El Niño years (1991, 1994, 1997, 2002, 2004, 2006, 2009, and 2015) in our study period, chosen as the 12 months (January–December) prior to the El Niño peak at the end of the calendar year. This 12-month period may be viewed as the onset and development phases of the event. However, the onset of La Niña events is often very abrupt, and a 12-month period prior to the La Niña peak may often include wind activity associated with the preceding El Niño. An extreme case is the 2010/11 La Niña. Westerly wind anomalies persisted during the first months of 2010, resulting in a wind evolution that may not be representative of La Niña onset conditions. For this reason we excluded this event from the analysis and chose the following eight La Niña years: 1995, 1998, 1999, 2000, 2005, 2007, 2008, and 2011. Some of these years are consecutive years associated with multiyear La Niña events, which we treated as independent events. Years that were not categorized as El Niño or La Niña years were considered neutral. Spectra for the individual El Niño, La Niña, and neutral years are highlighted in red, blue, and gray, respectively. The averages of the yearly El Niño and La Niña spectra are also shown. It is interesting that the 2014 spectrum (yellow curve) lies well within the range of neutral conditions. A relatively large spread is found in the low-frequency level of the yearly spectra. Nevertheless, it is evident that cold events generally tend to be associated with lower noise forcing levels than warm events. This is consistent with the linear dependence of the stochastic wind forcing amplitude on SST assumed in several studies as correlated additive and multiplicative (CAM) noise (Sardeshmukh and Penland 2015; Jin et al. 2007; Bianucci 2016), which is important for understanding the distinctively non-Gaussian nature of several large-scale atmospheric and oceanic variables.

It could be argued that the year-to-year differences among the spectra in Fig. 14a could simply be due to sampling, as yearly realizations of a red noise process similar to that described by Eq. (1b). To address this issue, we integrated Eq. (1b) for 7800 years to produce a synthetic time series that contained numerous realizations consistent with that red noise process. We first verified that the average spectrum computed from the 300 26-yr segments of the time series agreed with the original fit in Fig. 10b (light blue line in Fig. 10b) and then examined the spread of the 7800 yearly spectra. The 95% confidence intervals are indicated by the gray band in Fig. 14b. The observational spectra for most El Niño/ La Niña years in our study period fall within the gray band, indicating that differences among those spectra could indeed have just occurred by chance. However, the wind spectra for the years just preceding the 1997/98 and 2009/10 El Niño events exceed the 95% confidence level. For these cases, the null hypothesis that they originate from the sampling distribution of a red noise process may thus be rejected. The spectra in Fig. 14 also show that, on average, higher power at low frequencies corresponds to slightly higher power also at periods shorter than $\sim$100 days, consistent with the good correspondence between HF wind activity and ENSO seen in Fig. 15.

5. Summary and conclusions

In this study, we used a recently released observational wind vector dataset, in combination with SSH and SST data at high temporal resolution, to clarify the nature of the stochastic wind forcing of ENSO. This wind dataset provides a continuous record of 6-hourly values over a 26-yr period from January 1990 to December 2016, allowing a detailed characterization of equatorial winds from daily to interannual time scales.

We first examined the spectral characteristics of zonal winds along the equator and showed that they have comparable power in the central Pacific at interannual and subseasonal time scales. The latter includes the MJO at periods of 30–90 days, as well as its higher-frequency tail at periods shorter than 30 days. This high-frequency tail has typically been associated with westerly wind events (WWEs) that have been considered important triggers of El Niño through the excitation of subseasonal Kelvin waves. We found, however, that the high-frequency winds excite a Kelvin wave field that is much weaker than its low-frequency (interannual) counterpart. This indicates that it is the low-frequency component of the winds that is really important in forcing ENSO, in agreement with the simple paradigm presented in section 1. To illustrate this point, we showed that the main difference between the evolution of the 1997/98 and 2014/15 events was not due to differences in the high-frequency winds but rather in the low-frequency wind forcing.

In agreement with our simple paradigm, our results support the idea of the stochastic wind forcing of ENSO being not a purely high-frequency forcing but one that also has low-frequency power. The level of the low-frequency power shows some dependence on the ENSO state, supporting a possible role for a multiplicative noise forcing of ENSO suggested in several studies. We stress that the total low-frequency wind power comprises not only the deterministic response of the winds to the large-scale SST anomalies, but also the low-frequency tails of both the additive and multiplicative noise wind forcing components. The relative contributions of these different components, which have been estimated by several investigators using different approaches (Vecchi et al. 2006; Zavala-Garay et al. 2008; Levine et al. 2017), are still unclear. It is also unclear what factors control the development of the interannual wind variations like those observed during 1997 but almost absent during 2014. To what extent is the low-frequency atmospheric coupling influenced by large-scale climate conditions, including the magnitude of ENSO events? Also, to what extent are the large-scale climate variations favorable or unfavorable for generating strong stochastic wind forcing? These are still open questions.

El Niño events display large diversity in amplitude and spatial pattern (Capotondi et al. 2015), which has been related to differences in SST and thermocline precursors (Vimont et al. 2014; Capotondi and Sardeshmukh 2015), as well as to differences in dynamical feedbacks (Kug et al. 2009, 2010; Capotondi 2013). It has been suggested that the stochastic wind forcing may differ during epochs dominated by different ENSO types (Harrison and Chiodi 2009), but the origin, nature, and predictability of these differences are unknown.

We note that the efficacy of the stochastic wind forcing of ENSO is strongly influenced by the oceanic background conditions. Coupled model studies (Hu et al. 2014; Fedorov et al. 2015; Puy et al. 2018) have shown that the presence of WWEs can strongly influence the amplitude and type of El Niño events depending on subsurface ocean conditions. In particular, a state with enhanced upper oceanic heat content (a ''recharged'' ocean) would result in moderate El Niño events with largest amplitude in the central Pacific (CP events) in the absence of WWEs, but may develop, in the presence of WWEs, into a strong El Niño event with maximum SST anomalies in the eastern Pacific (EP event). Similarly, a ''discharged'' ocean would develop into a La Niña in the absence of WWEs, but may result in a CP El Niño in the presence of WWEs. The sign and amplitude of the resulting SST anomalies could be expected to influence the development of subsequent WWEs, and therefore the level of the stochastic wind variability.

We end by noting that while our high-resolution wind dataset is long enough to allow the impacts of the wind variability at different time scales to be investigated, it would obviously be desirable to have an even longer dataset to more adequately address the remaining open questions.

Acknowledgments. AC and LR were supported by the NASA Physical Oceanography Program (Award NNX15AG46G). The authors are grateful to Drs. C. Deser and P. Di Nezio for useful discussions during the early stages of this work and to G. Liguori for his invaluable help with the nonlinear fit of the wind spectrum. Three anonymous reviewers provided excellent and constructive comments that resulted in a greatly improved manuscript. The authors declare no conflicts of interest. CCMP version-2.0 vector wind analyses are produced by Remote Sensing Systems. Data are available at www.remss.com. AVISO SSH data were obtained from http://www.aviso.oceanobs.com/en/data/products/ and the OISST data from NOAA/ESRL/PSD (http://www.esrl.noaa.gov/psd/).

REFERENCES

Atlas, R., R. N. Hoffman, J. Ardizzone, S. M. Leidner, J. C. Jusem, D. K. Smith, and D. Gombos, 2011: A cross-calibrated, multiplatform ocean surface wind velocity product for meteorological and oceanographic application. *Bull. Amer. Meteor. Soc.*, **92**, 157–174, https://doi.org/10.1175/2010BAMS2946.1.

Bianucci, M., 2016: Analytical probability density function for the statistics of the ENSO phenomenon: Asymmetry and power law tail. *Geophys. Res. Lett.*, **43**, 386–394, https://doi.org/10.1002/2015GL066772.

Bjerknes, J., 1969: Atmospheric teleconnections from the equatorial Pacific. *Mon. Wea. Rev.*, **97**, 163–172, https://doi.org/10.1175/1520-0493(1969)097<0163:ATFTEP>2.3.CO;2.

Capotondi, A., 2013: ENSO diversity in the NCAR CCSM4 climate model. *J. Geophys. Res. Oceans*, **118**, 4755–4770, https://doi.org/10.1002/jgrc.20335.

——, and M. Alexander, 2001: Rossby waves in the tropical North Pacific and their role in decadal thermocline variability. *J. Phys. Oceanogr.*, **31**, 3496–3515, https://doi.org/10.1175/1520-0485(2002)031<3496:RWITTN>2.0.CO;2.

——, and P. D. Sardeshmukh, 2015: Optimal precursors of different types of ENSO events. *Geophys. Res. Lett.*, **42**, 9952–9960, https://doi.org/10.1002/2015GL066171.

——, M. A. Alexander, and C. Deser, 2003: Why are there Rossby wave maxima in the Pacific at 10°S and 13°N? *J. Phys. Oceanogr.*, **33**, 1549–1563, https://doi.org/10.1175/2407.1.

——, and Coauthors, 2015: Understanding ENSO diversity. *Bull. Amer. Meteor. Soc.*, **96**, 921–938, https://doi.org/10.1175/BAMS-D-13-00117.1.

Chelton, D. B., M. G. Schlax, M. H. Freilich, and R. F. Milliff, 2004: Satellite measurements reveal persistent small-scale features in ocean winds. *Science*, **303**, 978–983, https://doi.org/10.1126/science.1091901.

Chiodi, A. M., and D. E. Harrison, 2015: Equatorial Pacific easterly wind surges and the onset of La Niña events. *J. Climate*, **28**, 776–792, https://doi.org/10.1175/JCLI-D-14-00227.1.

Eisenman, I., L. Yu, and E. Tziperman, 2005: Westerly wind bursts: ENSO's tail rather than the dog? *J. Climate*, **18**, 5224–5238, https://doi.org/10.1175/JCLI3588.1.

Fedorov, A. V., S. Hu, M. Lengaigne, and E. Guilyardi, 2015: The impact of westerly wind bursts and ocean initial state on the development and diversity of El Niño events. *Climate Dyn.*, **44**, 1381–1401, https://doi.org/10.1007/s00382-014-2126-4.

Frankignoul, C., and K. Hasselmann, 1977: Stochastic climate models. Part II: Application to sea-surface temperature anomalies and thermocline variability. *Tellus*, **29**, 289–305, https://doi.org/10.3402/tellusa.v29i4.11362.

Gebbie, G., I. Eisenman, A. T. Wittenberg, and E. Tziperman, 2007: Modulation of westerly wind bursts: A semistochastic feedback of ENSO. *J. Atmos. Sci.*, **64**, 3281–3295, https://doi.org/10.1175/JAS4029.1.

Gill, A. E., 1982: *Atmosphere–Ocean Dynamics*. Academic Press, 662 pp.

Goldenberg, S. B., and J. J. O'Brien, 1981: Time and space variability of tropical Pacific wind stress. *Mon. Wea. Rev.*, **109**, 1190–1207, https://doi.org/10.1175/1520-0493(1981)109<1190:TASVOT>2.0.CO;2.

Harrison, D. E., and D. S. Luther, 1990: Surface winds from tropical Pacific islands—Climatological statistics. *J. Climate*, **3**, 251–271, https://doi.org/10.1175/1520-0442(1990)003<0251:SWFTPI>2.0.CO;2.

——, and G. A. Vecchi, 1997: Westerly wind events in the tropical Pacific, 1986–95. *J. Climate*, **10**, 3131–3156, https://doi.org/10.1175/1520-0442(1997)010<3131:WWEITT>2.0.CO;2.

——, and A. M. Chiodi, 2009: Pre- and post-1997/98 westerly wind events and equatorial Pacific cold tongue warming. *J. Climate*, **22**, 568–581, https://doi.org/10.1175/2008JCLI2270.1.

Hu, S., and A. V. Fedorov, 2016: Exceptionally strong easterly wind burst stalling El Niño of 2014. *Proc. Natl. Acad. Sci. USA*, **113**, 2005–2010, https://doi.org/10.1073/pnas.1514182113.

——, ——, M. Lengaigne, and E. Guilyardi, 2014: The impact of westerly wind bursts on the diversity and predictability of El Niño events: An ocean energetics perspective. *Geophys. Res. Lett.*, **41**, 4654–4663, https://doi.org/10.1002/2014GL059573.

Jin, F.-F., A. Timmermann, and J. Zhao, 2007: Ensemble-mean dynamics of the ENSO recharge oscillator under state-dependent stochastic forcing. *Geophys. Res. Lett.*, **34**, L03807, https://doi.org/10.1029/2006GL027372.

Julian, P., 1975: Comments on the determination of significance levels of the coherence statistic. *J. Atmos. Sci.*, **32**, 836–837, https://doi.org/10.1175/1520-0469(1975)032<0836:COTDOS>2.0.CO;2.

Kalnay, E., and Coauthors, 1996: The NCEP/NCAR 40-Year Reanalysis Project. *Bull. Amer. Meteor. Soc.*, **77**, 437–471, https://doi.org/10.1175/1520-0477(1996)077<0437:TNYRP>2.0.CO;2.

Kessler, W. S., and R. Kleeman, 2000: Rectification of the Madden–Julian oscillation into the ENSO cycle. *J. Climate*, **13**, 3560–3575, https://doi.org/10.1175/1520-0442(2000)013<3560:ROTMJO>2.0.CO;2.

Kug, J.-S., F.-F. Jin, K. P. Sooraj, and I.-S. Kang, 2008: State-dependent atmospheric noise associated with ENSO. *Geophys. Res. Lett.*, **35**, L05701, https://doi.org/10.1029/2007GL032017.

——, ——, and S.-I. An, 2009: Two types of El Niño events: Cold tongue El Niño and warm pool El Niño. *J. Climate*, **22**, 1499–1515, https://doi.org/10.1175/2008JCLI2624.1.

——, J. Choi, S.-I. An, F.-F. Jin, and A. T. Wittenberg, 2010: Warm pool and cold tongue El Niño events as simulated by the GFDL CM2.1 coupled GCM. *J. Climate*, **23**, 1226–1239, https://doi.org/10.1175/2009JCLI3293.1.

Lengaigne, M., E. Guilyardi, J. P. Boulanger, C. Menkes, P. Delecluse, P. Inness, J. Cole, and J. Slingo, 2004: Triggering of El Niño by westerly wind events in a coupled general circulation model. *Climate Dyn.*, **23**, 601–620, https://doi.org/10.1007/s00382-004-0457-2.

Levine, A. F. Z., and M. J. McPhaden, 2016: How the July 2014 easterly wind burst gave the 2015–2016 El Niño a head start. *Geophys. Res. Lett.*, **43**, 6503–6510, https://doi.org/10.1002/2016GL069204.

——, and F.-F. Jin, 2017: A simple approach to quantifying the noise–ENSO interaction. Part I: Deducing the state-dependency of the wind stress forcing using monthly mean data. *Climate Dyn.*, **48**, 1–18, https://doi.org/10.1007/s00382-015-2748-1.

——, ——, and M. F. Stueker, 2017: A simple approach to quantifying the noise-ENSO interaction. Part II: The role of coupling between the warm pool and equatorial zonal wind anomalies. *Climate Dyn.*, **48**, 19–37, https://doi.org/10.1007/s00382-016-3268-3.

Lopez, H., B. P. Kirtman, E. Tziperman, and G. Gebbie, 2013: Impact of interactive westerly wind bursts on CCSM3. *Dyn. Atmos. Oceans*, **59**, 24–51, https://doi.org/10.1016/j.dynatmoce.2012.11.001.

McGregor, S., A. Sen Gupta, D. Dommenget, T. Lee, M. J. McPhaden, and W. S. Kessler, 2017: Factors influencing the skill of synthesized satellite wind products in the tropical Pacific. *J. Geophys. Res. Oceans*, **122**, 1072–1089, https://doi.org/10.1002/2016JC012340.

McPhaden, M. J., 1999: Genesis and evolution of the 1997–98 El Niño. *Science*, **283**, 950–954, https://doi.org/10.1126/science.283.5404.950.

——, H. P. Freitag, S. P. Hayes, B. A. Taft, Z. Chen, and K. Wyrtki, 1988: The response of the equatorial Pacific Ocean to a westerly wind burst in May 1986. *J. Geophys. Res.*, **93**, 10 589–10 603, https://doi.org/10.1029/JC093iC09p10589.

Menkes, C. E., M. Lengaigne, J. Vialard, M. Puy, P. Marchesiello, S. Cravatte, and G. Cambon, 2014: About the role of westerly wind events in the possible development of an El Niño in 2014. *Geophys. Res. Lett.*, **41**, 6476–6483, https://doi.org/10.1002/2014GL061186.

Newman, M., and P. D. Sardeshmukh, 2017: Are we near the predictability limit of tropical Indo-Pacific sea surface temperatures? *Geophys. Res. Lett.*, **44**, 8520–8529, https://doi.org/10.1002/2017GL074088.

Penland, C., and P. Sardeshmukh, 1995: The optimal growth of tropical SST anomalies. *J. Climate*, **8**, 1999–2024, https://doi.org/10.1175/1520-0442(1995)008<1999:TOGOTS>2.0.CO;2.

Puy, M., J. Vialard, M. Lengaigne, and E. Guilyardi, 2016: Modulation of equatorial Pacific westerly/easterly wind events by the Madden–Julian oscillation and convectively-coupled Rossby waves. *Climate Dyn.*, **46**, 2155–2178, https://doi.org/10.1007/s00382-015-2695-x.

——, and Coauthors, 2018: Influence of westerly wind events stochasticity on El Niño amplitude: The case of 2014 vs. 2015. *Climate Dyn.*, https://doi.org/10.1007/s00382-017-3938-9, in press.

Reynolds, R. W., T. M. Smith, C. Liu, D. B. Chelton, K. S. Casey, and M. G. Schlax, 2007: Daily high-resolution blended analyses for sea surface temperature. *J. Climate*, **20**, 5473–5496, https://doi.org/10.1175/2007JCLI1824.1.

Ricciardulli, L., and Coauthors, Eds., 2017: The Climate Data Guide. CCMP: Cross-Calibrated Multi-Platform wind vector analysis. UCAR, accessed 2017, https://climatedataguide.ucar.edu/climate-data/ccmp-cross-calibrated-multi-platform-wind-vector-analysis.

Rong, X., R. Zhang, T. Li, and J. Su, 2011: Upscale feedback of high-frequency winds to ENSO. *Quart. J. Roy. Meteor. Soc.*, **137**, 894–907, https://doi.org/10.1002/qj.804.

Roulston, M. S., and J. D. Neelin, 2000: The response of an ENSO model to climate noise, weather noise, and intraseasonal forcing. *Geophys. Res. Lett.*, **27**, 3723–3726, https://doi.org/10.1029/2000GL011941.

Roundy, P. E., and G. N. Kiladis, 2006: Observed relationship between oceanic Kelvin waves and atmospheric forcing. *J. Climate*, **19**, 5253–5272, https://doi.org/10.1175/JCLI3893.1.

Sardeshmukh, P. D., and C. Penland, 2015: Understanding the distinctively skewed and heavy tailed character of atmospheric and oceanic probability distributions. *Chaos*, **25**, 036410, https://doi.org/10.1063/1.4914169.

Seiki, A., and Y. N. Takayabu, 2007: Westerly wind bursts and their relationship with intraseasonal variations and ENSO. Part I: Statistics. *Mon. Wea. Rev.*, **135**, 3325–3345, https://doi.org/10.1175/MWR3477.1.

Stuecker, M. F., A. Timmermann, F.-F. Jin, S. McGregor, and H.-L. Ren, 2013: A combination mode of the annual cycle and the El Niño/Southern Oscillation. *Nat. Geosci.*, **6**, 540–544, https://doi.org/10.1038/ngeo1826.

Trenberth, K. E., 1984: Some effects of finite sample size and persistence on meteorological statistics. Part I: Autocorrelations. *Mon. Wea. Rev.*, **112**, 2359–2368, https://doi.org/10.1175/1520-0493(1984)112<2359:SEOFSS>2.0.CO;2.

Tziperman, E., and L. Yu, 2007: Quantifying the dependence of westerly wind bursts on the large-scale tropical Pacific SST. *J. Climate*, **20**, 2760–2768, https://doi.org/10.1175/JCLI4138a.1.

Vecchi, G. A., A. T. Wittenberg, and A. Rosati, 2006: Reassessing the role of stochastic forcing in the 1997–98 El Niño. *Geophys. Res. Lett.*, **33**, L01706, https://doi.org/10.1029/2005GL024738.

Vimont, D., M. A. Alexander, and M. Newman, 2014: Optimal growth of central and east Pacific ENSO events. *Geophys. Res. Lett.*, **41**, 4027–4034, https://doi.org/10.1002/2014GL059997.

Wentz, F. J., J. Scott, R. Hoffman, M. Leidner, R. Atlas, and J. Ardizzone, 2015: Remote Sensing Systems Cross-Calibrated Multi-Platform (CCMP) 6-hourly ocean vector wind analysis product on 0.25° grid, version 2.0. Remote Sensing System, accessed 2017, www.remss.com/measurements/ccmp.

Wittenberg, A. T., 2004: Extended wind stress analyses for ENSO. *J. Climate*, **17**, 2526–2540, https://doi.org/10.1175/1520-0442(2004)017<2526:EWSAFE>2.0.CO;2.

Yu, L., R. A. Weller, and T. W. Liu, 2003: Case analysis of a role of ENSO in regulating the generation of westerly wind bursts in the western equatorial Pacific. *J. Geophys. Res.*, **108**, 3128, https://doi.org/10.1029/2002JC001498.

Zavala-Garay, J., C. Zhang, A. M. Moore, A. T. Wittenberg, M. J. Harrison, A. Rosati, J. Vialard, and R. Kleeman, 2008: Sensitivity of hybrid ENSO models to unresolved atmospheric variability. *J. Climate*, **21**, 3704–3721, https://doi.org/10.1175/2007JCLI1188.1.

Zhang, C. D., and J. Gottschalck, 2002: SST anomalies of ENSO and the Madden–Julian oscillation in the equatorial Pacific. *J. Climate*, **15**, 2429–2445, https://doi.org/10.1175/1520-0442(2002)015<2429:SAOEAT>2.0.CO;2.